A Reexamination of Latitudinal Limits of Substorm-Produced Energetic Electron Precipitation

Kathy Cresswell-Moorcock and Craig J. Rodger

Department of Physics, University of Otago, Dunedin, New Zealand

Antti Kero

Sodankylä Geophysical Observatory, University of Oulu, Sodankylä, Finland

Andrew B. Collier

SANSA Space Science, Hermanus, South Africa

Mark A. Clilverd

British Antarctic Survey (NERC), Cambridge, United Kingdom

Ingemar Häggström

EISCAT Scientific Association, Kiruna, Sweden

Timo Pitkänen

Department of Physics, University of Oulu, Oulu, Finland

Abstract. The primary sources of energetic electron precipitation (EEP) which affect altitudes <100 km (>30 keV) are expected to be from the radiation belts, and during substorms. EEP from the radiation belts should be restricted to locations between *L*=1.5-8, while substorm produced EEP is expected to range from *L*=4-9.5 during quiet geomagnetic conditions. Therefore, one would not expect any significant D-region impact due to electron precipitation at geomagnetic latitudes beyond about *L*=10. In this study we report on large unexpectedly high latitude D-region ionization enhancements, detected by an incoherent scatter radar at *L*≈16, which appear to be caused by electron precipitation from substorms. We go on to reexamine the latitudinal limits of substorm produced EEP using data from multiple low-Earth orbiting spacecraft, and demonstrate that the precipitation stretches many hundreds of kilometers polewards of the previously suggested limits. We find that a typical substorm will produce significant EEP over the IGRF *L*-shell range *L*=4.6±0.2-14.5±1.2, peaking at *L*=6-7. However, there is significant variability from event to event; in contrast to the median case, the strongest 25% of substorms have significant EEP in the range spaning *L*=4.1±0.1-20.7±2.2, while the weakest 25% of substorms have significant EEP in the range spaning *L*=5.5±0.1-10.1±0.7. We also examine the occurrence probability of very large substorms, focusing on those events which appear to be able to disable geostationary satellites when they are located near midnight MLT. On average these large substorms occur approximately 1-6 times per year, a significant rate given the potential impact on satellites.

1. Introduction

Magnetospheric substorms (henceforth referred to as substorms) are brief disturbances in the magnetosphere in response to a time limited increase in energy input from the solar wind to the magnetosphere. They are linked to the southward turning of the *z* component of the Interplanetary Magnetic Field (IMF) [e.g., *Akasofu*, 1981] (also described as "IMF negative") and to the presence of high solar wind speeds [e.g., *Tanskanen et al.*, 2005], although substorms have been known to occur when these conditions are not met [*Rostoker et. al.*, 1980]. Substorms are significant space weather events, involving the reconfiguration of the magnetic fields in the magnetosphere, plasma flows in the magnetotail, the generation of electromagnetic waves in the inner magnetosphere, and particle precipitation into the ionosphere ranging from auroral to relativistic energies. While the various phenomena occurring during substorms are fairly well documented, the order of the events leading to the substorm onset is still under some dispute [e.g., *Nishimura et al.*, 2010; *Liu et al.*, 2012].

While comparatively common, with several substorms occurring in a typical day, large substorms have been associated with effects as dramatic as the loss of control of the Galaxy 15 geostationary communications satellite in April 2010 [*Connors et al.*, 2011; *Clilverd et al.*, 2012b].

Substorms generate energetic electron precipitation (EEP) through the conversion of solar wind energy stored in the Earth's magnetotail into particle heating and kinetic energy, part of which is seen in the ionosphere as brightenings of aurorae [e.g. *Akasofu*, 1964; *Axford*, 1999; *Liu et al.*, 2009]. *Spanswick et al.* (2009) studied a substorm on 27 August 2001 in detail, concluding that EEP was observed on the ground near $L = 6.6$ and it expanded both polewards and equatorwards - consistent with the earlier riometer-based survey of *Berkey et al.* [1974]. Typically, EEP from a substorm starts near magnetic midnight, with the ionospheric precipitation region rapidly expanding eastwards with velocities that correspond to electron drift velocities associated with energies of 50-300 keV [*Berkey et al.*, 1974]. The electron energies involved in substorm injections seen by satellites such as LANL are typically 50-1000 keV, with the highest fluxes occurring at the lowest energies [*Clilverd et al.*, 2008, *Rodger et al.*, 2012]. Recent papers have suggested that a very large fraction of the enhanced population of energetic electrons (50-1000 keV) observed by geostationary satellites during substorms precipitates into the atmosphere. *Clilverd et al.* [2008] concluded that roughly 50% of the electrons injected near the LANL-97A satellite during a substorm on 1 March 2006 precipitated in the region near the satellite, and comparable EEP fluxes were reported by *Clilverd et al.* [2012a] for another THEMIS detected-substorm occurring on 28 May 2010. Both of these studies combined the satellite measurements with observations from a riometer and subionospheric VLF instruments. In addition, *Watson et al.* [2011] examined GPS total electron content (TEC) measurements during substorms and reported vertical TEC changes of several TEC units associated with the substorm. By studying the apparent expansion of the precipitation region due to the substorm, they concluded that the bulk of the vertical TEC change occurred at altitudes of approximately ~100 km, i.e., the vertical TEC was responding to the EEP and not the very considerable population of <1 keV electrons that also precipitate during substorms [*Mende et al.*, 2003]. This conclusion was found to be consistent with the observed responses of the ionospheric D-region to EEP observed by riometer and subionospheric VLF instruments during large substorm EEP events [*Rodger et al.*, 2012].

Precipitating charged particles produce odd nitrogen and odd hydrogen in the Earth's atmosphere which can catalytically destroy ozone [*Brasseur and Solomon*, 2005]. As a result, EEP events have been linked to significant decreases in polar ozone observed in the upper stratosphere [e.g., *Randall et al.*, 2007; *Seppälä et al.*, 2007]. By influencing stratospheric ozone variability in the polar region, energetic particle precipitation can affect the stratospheric radiative balance, and may link to significant polar surface climate variability [*Rozanov et al.*, 2005; *Seppälä et al.*, 2009]. Recent experimental studies have demonstrated the direct production of odd nitrogen [*Newnham et al.*, 2011] and odd hydrogen [*Verronen et al.*, 2011; *Andersson et al.*, 2012] in the mesosphere by EEP.

Substorms are comparatively common; the annual mean substorm rate has been reported at 1400 per year [*Smith et al.*, 1996]. The events typically last 30 min – 2 hours. In addition, the peak EEP fluxes for some events can be several orders of magnitude larger than EEP from radiation belt processes [e.g., *Rodger et al.*, 2012], with precipitation also occurring at very high latitudes. Therefore, substorms may be an important contributor to EEP-produced polar atmospheric chemical changes, adding to both the "indirect effect" [*Randall et al.*, 2007] and direct change in the mesosphere [e.g., *Turunen et al.*, 2009; *Verronen et al.*, 2011; *Andersson et al.*, 2012]. As such it is important to accurately determine the latitude range over which substorm EEP will occur.

Substorm EEP events were comprehensively mapped by *Berkey et al.* [1974] using about 40 Northern Hemisphere riometers in the International Quiet Sun Year (1964–1965) and

International Active Sun Year (1969) to examine 60 substorms. Substorm events were selected where the nightside riometer record had been undisturbed for 1 hour before the onset of the substorm, the onset was abrupt with a rate of increase of absorption of at least 1 dB per 5 minutes, the duration of the absorption event was greater than 30 min and the absorption exceeded 1 dB for more than 5 minutes. The latitudinal extent of the EEP was then determined from the riometer observations using an absorption threshold of >0.3 dB. Initially the riometer absorption maxima were found to be located close to 65º geomagnetic invariant latitude (*L*~6). Within 15 min the zone then expanded to cover a corrected geomagnetic (CGM) latitude range of 60–74º, with a small dependence upon Kp. This EEP latitude range was found to be consistent with the observations from particle detectors on DMSP flights [*Sandholt et al.*, 2002].

The primary sources of EEP which affect altitudes <100 km are expected to be from the radiation belts and substorms. EEP from the radiation belts should be restricted to locations between *L*=1.5-8, while substorm produced EEP is expected to range from *L*=4-9.5 for low Kp conditions. Therefore, outside of solar proton events one would not expect any significant D-region impact due to precipitation at geomagnetic latitudes beyond about *L*=10. In this study we report on large high latitude D-region ionization enhancements detected by an incoherent scatter radar at a CGM latitude of 75.43° (*L*=16) which unexpectedly appear to be caused by substorms. We go on to reexamine the latitudinal limits of substorm produced EEP using data from multiple low-Earth orbiting spacecraft, and demonstrate that the precipitation stretches many hundreds of kilometers polewards of the previously suggested limits. We undertake a detailed analysis of substorm characteristics, and attempt to understand how and why the classical picture of substorm latitudinal extent does not include high latitudes such as those of the Svalbard incoherent scatter radar site.

2. D-Region enhancements during the IPY

2.1 EISCAT Svalbard Observations

During the International Polar Year (IPY) the EISCAT Svalbard Radar (ESR; 78.15°N, 16.02°E, CGM latitude 75.43°, IGRF L=15.7 at 100 km altitude) observed the ionosphere, including the D region, near-continuously from 1 March 2007 to 28 February 2008. This period was in the deep solar minimum, i.e., during low solar activity, and no solar proton events occurred. One of the goals of this IPY campaign was to monitor the descent of thermospheric NOx produced by auroral precipitation into the mesosphere [*Clilverd et al.*, 2006; *Randall et al.*, 2007]. A summary of the physics of incoherent scatter radar systems, like EISCAT, can be found in *Kofman* [1992].

As noted above, the *Berkey et al.* [1974] study considered the typical poleward and equatorward boundaries for significant substorm produced precipitation as defined by a >0.3 dB riometer absorption threshold. That study made use of corrected geomagnetic latitude values, and reported that the poleward threshold was 71° latitude for Kp<5 (with little local time dependence), and 71-74° for Kp=6-7, depending on local time, but not solar activity levels. During the IPY geomagnetic activity was typically very low, and the Kp-excursions which occurred were generally small. Thus the lower Kp boundary is more appropriate for our study, as will be confirmed later. Figure 2 and 3 of *Berkey et al.* [1974] give a contour map of the CGM latitude contours used in their analysis. We find that the outer CGM limit of 71° calculated for 1969 corresponds well with the IGRF L-shell contour of 9.5, and is consistent with Figure 2 of *Berkey et al.* [1974]. In our study we will work primarily in IGRF-L-shells as the POES dataset we use in a later section includes the IGRF L-shell with high-time resolution. In IGRF L-shells the *Berkey et al.* [1974] limits for the >0.3 dB riometer absorption span L=4 to 9.5 for geomagnetic disturbances from 2<Kp<6.

Figure 1 shows the location of the ESR (green star) as well as the L-shell limits for significant substorm EEP determined by *Berkey et al.*, [1974] and the radiation belt EEP limits suggested above. Clearly, the ESR facility is well beyond the outer edge of the L≈9.5 substorm EEP limit (in terms of significant EEP during the *Berkey et al.* [1974] substorms), in practice about ~500 km further polewards. As noted above, the location of the ESR is such that one would not typically expect any significant D-region ionization changes due to particle precipitation except during solar proton events, as it is located well poleward of the expected locations for EEP from the radiation belts or the substorms reported by *Berkey et al.* [1974].

It was therefore unexpected when a set of sharp D-region electron density changes were observed in the ESR data, clearly not associated with known D-region triggers (e.g., X-rays from solar flares), and leading to a more detailed investigation reported here. The ESR electron number density dataset was analyzed using 1 minute and 3 km altitude resolutions looking for sudden changes in D-region density. The identification criterion for an event used was that the electron number density in the 80-100 km altitude range increased suddenly for 5 minutes by 5 times the preceding (5 minute median) level. This criterion will select only very clear cases, preferentially identifying the initial onset from quiet conditions, and missing many weak events or even strong ones taking place in the middle of disturbed conditions. However, it provides a dataset of well-defined events for us to examine further. In this way 112 events were identified. Figure 2 shows a superposed epoch analysis (SEA) of the 112 IPY ESR events; the left-hand panel shows the statistical mean while the right hand panel shows the statistical median. We only consider EISCAT electron number density observations for altitudes above 70 km as sea reflections and multipath propagation can lead to spurious results at lower altitudes. Figure 2 demonstrates that the IPY ESR events have consistent and clear responses which will in part reflect the event selection criteria. A typical "quiet" level of electron number density is visible before the event epoch, with a sudden increase of 1-2 orders of magnitude in electron density directly at epoch which occurs over a wide range of altitudes (and certainly ~75-100 km). The increased electron density weakens over a period of approximately one hour before returning to typical quiet levels.

2.2 The question of substorm-EEP

The left hand panel of Figure 3 shows the Magnetic Local Time (MLT) variations of the IPY ESR electron number density increase events (henceforth "IPY ESR events"). Clearly, the IPY ESR events are strongly clustered around magnetic midnight, which is the first suggestion that these unexpected events might be caused by substorm-EEP, which we consider in more detail below. The right hand panel of Figure 3 shows a superposed epoch analysis (SEA) of the *z*-component of the IMF for the epochs defined by the IPY ESR events (henceforth "IPY ESR epochs"). The IMF observations were provided by the Advanced Composition Explorer (ACE) satellite and time shifted to allow for the travel time from the satellite position to the Earth's magnetosphere. In this figure the superposed epoch median of the IMF B_z is given by a black line while the 95% confidence interval for the median is given by the red band. Dark blue bands mark the interquartile range and the 95% confidence interval about it (light blue). Clearly, ~1-2 hours before the IPY ESR epochs there is a highly repeatable southward turning in the IMF, which is of a similar magnitude to that seen for substorms (not shown). The majority of the IPY ESR events occur during periods of high solar wind speeds which, as previously noted, is also expected for substorms. Further superposed epoch analysis of these events (not shown) show they are associated with small decreases in the median Dst index (to about -13.5 nT), a brief upward spike in AE (to 250 nT) and a small disturbance in Kp (up to ~3), which are also all very similar to those observed for known substorm events. A manual investigation was made of the AL and IL indices (the latter similar to AL but produced using the IMAGE magnetometer chain) around the times of the IPY ESR events. This confirmed that the majority of events occurred during the expansion phase or recovery phase of substorms detected in one or both of these indices. The small Kp disturbance associated with these events also confirms that, on the basis of the *Berkey et al.* [1974] latitude limits noted above, one would not expect significant substorm produced EEP above this location.

One known signature of energetic particle acceleration occurring during substorms is the sudden appearance of "dispersionless injections" in particle observations made near geosynchronous orbit [e.g., *Sarris and Li*, 2005]. We therefore examine geosynchronous satellite particle data from the SOPA instrument on the LANL spacecraft which have previously been used to characterize substorms and link them to substorm EEP [e.g., *Clilverd et al.*, 2008]. Note that the LANL spacecraft data are now closed to non-military scientific use, and we are therefore limited to examining the IPY ESR epochs in 2007 for which we already had the data available. Seventy seven of the IPY ESR events occurred in 2007, and there is SOPA/LANL geostationary observations for 75 of these events. Two thirds of these showed an injection, consistent with the occurrence of a substorm. However, we cannot state that the remaining 25 IPY ESR 2007 events were not substorms; another known signature for substorms is a fast narrow flow burst from the magnetotail caused by magnetic reconnection. Recent comparisons between SOPA/LANL injections and flow bursts observed by Geotail and THEMIS found that only about one-third of flow bursts led to LANL-detected injections [*Sergeev et al.*, 2012].

The evidence above suggests that the IPY ESR events are indeed due to substorm EEP, despite the high-latitude of the ESR facility. One possibility as to why *Berkey et al.* [1974] did not include substorm EEP events similar to the IPY ESR events is that the Svalbard EEP flux magnitudes might be too small to produce a >0.3 dB riometer absorption change. We have tested this by determining the riometer absorption which would be produced by the median ESR-observed electron number density variations shown in the right hand panel of Figure 2. Following the calculation approach outlined in *Rodger et al.* [2012] we find the increase in riometer total absorption for the median 70-100 km altitude ionization changes observed in the IPY ESR events is ~0.59 dB, and thus one would expect these events would have been included in the *Berkey et al.* [1974] study and thus moved the poleward edge for significant precipitation during weak substorms closer to the pole.

However, one might also speculate that the difference between the mapped footprints of the field-lines associated with L=10 and L=16 is rather small and might not have been differentiated by the *Berkey et al.* [1974] study, even though we have indicated it is ~500 km. We therefore turn to low-Earth orbiting satellite data to provide an alternative determination of the geomagnetic latitude limits for substorm-EEP.

3. Satellite instrumentation and data

3.1 POES Satellite Data

Here we utilize the second generation Space Environment Module (SEM-2) [*Evans and Greer*, 2004] flown on the Polar Orbiting Environmental Satellites (POES) series of satellites, and on the Meteorological Operational (MetOp)-02 spacecraft. For our IPY ESR study period there are five satellites that carry the SEM-2 instrument package. These spacecraft are in Sun-synchronous polar orbits with typical parameters of ~800−850 km altitude, 102 min orbital period and 98.7° inclination [*Robel*, 2009]. The orbits typically are either morning or afternoon daytime equator crossings, with corresponding night-time crossings. Table 1 contains a summary of the SEM-2 carrying spacecraft operational at the time of writing.

We use SEM-2 Medium Energy Proton and Electron Detector (MEPED) observations from the NOAA-15 through 18 satellites plus the MetOp-2 satellite which also carries an SEM-2. All POES data are available from http://poes.ngdc.noaa.gov/data/ with the full-resolution data having 2-s time resolution. Analysis by *Rodger et al.* [2010a] indicated that the levels of contamination by comparatively low energy protons can be significant in the MEPED observations. As much as ~42% of the 0° telescope >30 keV electron observations were typically found to be contaminated, although the situation was less marked for the 90° telescope (3.5%). However, NOAA has developed new techniques to remove the proton contamination from the POES SEM-2 electron observations, as described in Appendix A of *Lam et al.* [2010]. This algorithm is available for download through the Virtual Radiation Belt Observatory (ViRBO; http://virbo.org).

The SEM-2 detectors include integral electron telescopes with energies of >30 keV (e1), >100 keV (e2), and >300 keV (e3), pointed in two directions. The 0º-pointing detectors are mounted on the three-axis stabilized POES spacecraft so that the centre of each detector field of view is outward along the local zenith, parallel to the Earth-centre-to-satellite radial vector. Another set of telescopes, termed the 90º-detectors, is mounted approximately perpendicular to the 0° detector, directed towards the wake of the satellite. The telescopes pointing in the 0º and 90º directions are ±15º wide. In the current study we only consider the observations from the 0° telescopes, using the channels summarized in Table 2. Modeling work has established that the 0° telescopes monitor particles in the atmospheric bounce loss cone that will enter the Earth's atmosphere below the satellite when the spacecraft is poleward of L≈1.5-1.6 [*Rodger et al.*, Appendix A, 2010b].

Before undertaking superposed epoch analysis we first combine the POES reported particle fluxes varying with L and time, using 0.25-L and 15-min time resolution. As such there can be a variable number of observations from a varying number of satellites included in each 0.25-L and 15-min time resolution bin. We grid the POES observations out to an IGRF L-shell of 30, as this should include all likely substorm precipitation. Observations from inside and around the South Atlantic Magnetic Anomaly are excluded before the measurements are combined. Solar proton events can render all POES electron observations meaningless, but as none occurred in the time period considered here this is not a concern.

3.2 SuperMAG list of Substorm Events

Identification of substorms can be somewhat challenging as different researchers focus upon different instruments and criteria for their definition of a substorm. In this study, we choose to use the substorm identification criteria of the SuperMAG collaboration of organizations and national agencies, whose list of substorm events is analyzed alongside our D-region and EEP observations. SuperMAG uses ground-based magnetometer chains of more than 100 observatories to derive an index that is similar to that used to define the AE index. The large number of observatories used by SuperMAG allows for greater coverage of the latitude range and much smaller time gaps. The automated algorithm to identify substorm expansion phase onsets from the SuperMAG observations has been described and validated [*Newell & Gjerloev*, 2011a, b], with the events available for download online through http://supermag.jhuapl.edu/substorm/.

4. SEA of IPY ESR events

As a first step, we undertake SEA of the POES precipitating electron and proton observations for the epochs defined by the 112 IPY ESR events, i.e., the times at which EISCAT reported D-region enhancements. We limit ourselves to POES observations made in the MLT region from 19-6 MLT, as this covers the majority of the ESR-observed events (Figure 3, left hand panel). The left hand panel of Figure 4 shows the SEA analysis of the >30 keV precipitating electrons observed by POES for these epochs and MLT range. There is a sharp increase by 1.5-2 orders of magnitude in the observed precipitating fluxes from L=5-14 at the times of the EISCAT derived epochs, consistent with the D-region observations being due to EEP. The dotted white horizontal line marks the L-shell of the ESR; clearly EEP is enhanced at these L-shells, as well as at yet higher magnetic latitudes. In order to quantify the significance of these observations, the right hand panel of Figure 4 shows the ratio of the SEA analysis in the left hand panel to that for a set of random time periods. The random epoch list is from the time period of the IPY ESR observations (1 March 2007 to 28 February

2008), where the MLT variation was taken from the IPY ESR epoch distribution shown in Figure 2, with the day number randomized. The right hand panel of Figure 4 demonstrates that while the >30 keV EEP is enhanced by 1.5-2.5 orders of magnitude around the epochs times, this occurs within a longer period of smaller enhanced EEP fluxes (0.5-1 orders of magnitude). This lower-level EEP enhancement spans ±1.5 days around the epoch and roughly corresponds to the time period in which the SEA of the solar wind speed is enhanced (>450 km/s; not shown).

As noted in Table 2, the SEM-2 instrument has multiple precipitating electron and proton energy ranges. For 0E1 to 0E3 and 0P1 to 0P3 the SEA plots are visually similar (not shown), but with smaller EEP enhancements relative to the random analysis at epoch time. For example, while the peak in the 0E1 ratio plot (right hand side of Figure 4) is ~350, this value is ~13 for 0E2 and a very marginal response in 0E3 suggesting higher energy electron precipitation is close to the noise floor of the instrument. For the precipitating particle channels (0E and 0P), we see no response at the ESR *L*-shell for the E3 and P5 channels, but do for lower energy ranges. We therefore conclude that the energy range for particles precipitating into the atmosphere above the ESR is ~30-300 keV for electrons and estimate the rough precipitation range for protons as being 30-800 keV on the basis of the response in the different 0P channels. Protons with energies <1 MeV will deposit the majority of their energy in the atmosphere above 95 km, while the 30-300 keV electrons will cause ionization rate enhancements down to about 70 km altitude [*Turunen et al.*, Fig. 3, 2009]. It is therefore most likely that the precipitation above Svalbard, which was seen in the IPY ESR data, is solely due to the precipitation of ~30-300 keV electrons.

Having examined the POES-precipitation observations at the times of the ESR observed D-region enhancements, we now use POES to confirm that these events are indeed substorm-driven.

5. SEA of SuperMAG Substorms

This is undertaken using the SuperMAG list of substorm events in the time period 1 March 2007 to 28 February 2008, which we will term the IPY substorm epochs. This list includes 1413 events in comparison with the 112 events in the IPY ESR epoch list. Substorm produced EEP evolves with time, geomagnetic latitude and MLT (see for example Figure 9 of *Berkey et al.* [1974]), and thus we analyse the SuperMAG substorm epochs for 4 different MLT regions. In our SEA we limit ourselves to POES observations made in the ±3 MLT regions centered on 0, 6, 12, and 18 MLT, as shown in Figure 5. We note that the SEA of the POES-observed >30 keV electron precipitation using the IPY substorm epochs centered on 0 and 6 MLT (upper panels of Figure 5) are visually extremely similar to that made using the IPY ESR epochs (Figure 4), although with a more clearly resolved pattern due to the larger number of epochs included in the SEA. Figure 5 shows that there are significant >30 keV enhancements immediately following the substorm onset, peaking ~30 min later in the 3-9 MLT sector. While substorm EEP clearly grows in IGRF *L*-value in the 0 MLT sector, this is most pronounced in the 6 MLT sector, where enhanced precipitation clearly extends beyond the L-shell of the ESR instrument. In the noon sector (12 MLT) the >30 keV enhancements are delayed relative to substorm onset, but also span a wide L-shell range and are long lived. In contrast, there is little enhancement in the precipitation in the 18 MLT sector. The general MLT features seen in Figure 5 are consistent with that reported by *Berkey et al.* [1974] (and in particular Figure 9 of that paper), except that the EEP stretches to higher geomagnetic latitude than reported in that study. Note that the long-lived enhanced >30 keV EEP well before the SuperMAG epoch is primarily due to substorms occurring in clusters during periods of high speed solar wind and thus appearing around the epoch time; a SEA considering only isolated substorms (±6 hours) does not include this feature.

The peak EEP timing in the SuperMAG SEA occurs ~1 hour later in contrast with the IPY ESR epochs, which is most likely a result of how the two epochs are determined. Part of this may result from the time taken for the substorm region to grow in latitudinal extent from its starting point around L≈6. The precipitating >30 keV fluxes observed in the SuperMAG substorm case are approximately 0.5-1 orders of magnitude (i.e., a factor of 3-10) weaker than for the ESR event case. Nonetheless, it is again clear that the ESR-observed D-region enhancements are due to substorm-triggered precipitation of energetic electrons, and that substorm precipitation is enhanced beyond L=10.

6. Latitudinal Limits for Substorm EEP

The SEA analysis of POES data presented above essentially confirms that the D-region enhancements observed by EISCAT were produced by substorm-triggered energetic electron precipitation, and thus that significant quantities of substorm EEP affect the ionosphere at geomagnetic latitudes beyond L=10. However, while a visual inspection of Figure 5 suggests that substorms typically boost EEP out to perhaps L≈16, this limit is rather arbitrary. We therefore consider the earlier threshold approach taken by *Berkey et al.* [1974]. Thus we take the limits for substorm EEP to be defined by the IGRF L-shells for which the EEP-produced D-region change for an average substorm leads to an additional riometer absorption of 0.3 dB.

As noted previously, we found that the median IPY ESR superposed epoch analysis of the electron number density changes would have been associated with a change in the cosmic noise absorption (ΔCNA) of ~0.59 dB, with the typical ΔCNA for a sunlit ionosphere being 1.4 dB and that for a dark ionosphere being 0.54 dB. We can also follow the approach outlined in *Rodger et al.* [2012] to calculate the ΔCNA from a given EEP flux. We make use of the peak POES-reported >30 keV precipitating electron flux at the L-shell of the ESR facility (Figure 4), and assume that the 30 keV-2.5 MeV EEP energy spectrum is described by a power law with slope -3.66 (after *Clilverd et al.* [2012a]), which agrees fairly well with the spectra from the POES superposed epoch analysis. We make our calculations for local midnight at the spatial location of the ESR facility, and assume a dark ionosphere. For the peak POES-reported >30 keV shown in Figure 4 for the ESR L-shell (3×10^{3} el. $cm^{-2}s^{-1}sr^{-1}$) the riometer ΔCNA is calculated to be only 0.01 dB, which is clearly negligible. This is, however, expected. Our SEA of the POES data combines the observations from multiple operational SEM-2 carrying satellites, most of which will not be located near the location of the substorm EEP; indeed, given the short lifetime of substorms it is quite likely that the POES instruments will only sample some part of the event and will not be present at the time and place where the EEP peaks. Thus we need to employ a "calibration factor" to correct for this. While this factor will be inappropriate to describe the conversion on an event basis, it should be valid when considering the statistical whole. We find that we need to boost the POES -reported >30 keV precipitating electron fluxes by a factor of 200 to produce a riometer ΔCNA of 0.54 dB. We therefore assume that 200 is a reasonable value to transform the POES SEA EEP observations to determine the ionospheric response. Note the calibration factor is not necessarily a meaningful geophysical parameter, but is necessary to undertake a statistical comparison between the POES observations, the ESR electron density profiles, and the Berkey riometers observations. For the ESR electron density profiles and the earlier Berkey riometers observations, the instruments were sampling continuously while not in motion. For POES, the measurements are obviously on a moving platform which will rapidly move through the L-shell and MLT region inside which the substorm EEP takes place. The conversion factor and statistical SEA process allows us to incorporate the brief sampling by the POES satellites of any given substorm event, and produce a meaningful estimate of its ionospheric significance and spatial size.

Figure 5 demonstrated that the majority of the substorm EEP occurs in the MLT range from 21-15 MLT. Thus in order to determine the typical L-shell limits for substorm EEP we use the peak >30 keV electron precipitation fluxes from a SEA undertaken using the POES data for this MLT range, representing the median EEP during SuperMAG-reported substorms, and calculate the ΔCNA after the fluxes have been increased by a factor of 200. The blue line in the lefthand panel of Figure 6 shows the results of this calculation. The ΔCNA peaks at L=6.9 with a value of 4.9 dB. The horizontal magenta dashed line marks the 0.3 dB threshold value. We assume that the L-shells in which the ΔCNA is above this threshold are "significant", and the vertical blue dashed lines mark the lower and upper limits for the median SEA analysis shown in Figure 5. In this case the EEP range spans IGRF L-shells from L=4.5-15.7. Note that these "typical" substorms are on the borderline producing "significant" EEP at the L-shell of the ESR facility at L=15.7. To clarify, here we define a typical substorm through the median observed EEP for a SUPERMAG substorm event determined using SEA. The red and green lines in Figure 6 shows ΔCNA calculated for the POES upper quartile (UQ) and lower quartile (LQ) observations, otherwise following the same route as outlined for the median events. While the upper quartile events form a restricted dataset, 25% of the total SuperMAG list is still 325 substorms, a considerable number to examine. In contrast to the median case, the strongest 25% of substorms have significant EEP in the range spanning L=3.95-22.9 (red line), while the weakest 25% of substorms have significant EEP in the range spanning L=5.3-10.8 (green line). This finding is consistent with Figures 4 and 5, which suggest that the IPY ESR events typically involve stronger EEP fluxes than the SuperMAG substorm list; higher flux substorms span a wider L-shell range and are thus more likely to produce detectable EEP above Svalbard.

As noted above, the "calibration factor" of 200 employed to produce the left hand panel of Figure 6 produces typical ΔCNA values of 4.9 dB. In contrast, however, the typical peak substorm absorption reported by *Berkey et al.* [Fig. 9, 1974] is closer to 3 dB, rather than ~5 dB. Note that this set of substorms included some events which occurred during more geomagnetic disturbed conditions which might affect the estimate peak value. However, we note that Figure 8 of *Berkey et al.* [1974] includes a case-study example for quieter geomagnetic conditions (Kp≤4), which peaks at 3 dB. This might suggest that the SuperMAG substorms are a strong subset of the total population (where strong refers to the magnitude of the EEP), or it may reflect errors behind the assumptions in our ESR to POES calibration approach. As an alternative technique, we assume that the typical peak substorm absorption should be 3 dB, which implies a calibration factor of 71 instead of 200. The result of this calculation is shown on the right hand side of Figure 6. The smaller ΔCNA mean that a smaller L-shell region experiences significant EEP levels. For the median case with calibration factor determined by the 3 dB peak, the EEP range spans IGRF L-shells from *L*=4.8-13.25, while it is 4.2-18.5 for the strongest 25% of substorms and 5.7-9.4 dB for the weakest 25%.

We assume that these two approaches provide indications of the position and uncertainty in the IGRF *L*-shell limits for substorm EEP, and thus determine the typical limits as spanning from *L*=4.6±0.2 to 14.5±1.2, while the strongest 25% of substorms span *L*=4.1±0.1 to 20.7±2.2 and the weakest 25% of substorms span 5.5±0.2 to 10.1±0.7. In practice our IGRF *L*-shell limits for typical substorm EEP are rather similar to those determined earlier by *Berkey et al.* [1974] from ground-based observations (*L*=4–9.5), noting that the variation across the dataset is large when comparing the median limits with those for the lower quartile and upper quartile. Given there is a significant difference in the calibration factor between the approaches, we acknowledge that our approach may only provide an order of magnitude estimate of the EEP flux magnitudes. Part of this stems from the small amount of time that the POES spacecraft sample the high latitude regions we focus on in this paper. For the determination of the calibration factor we make by comparison with ESR observations there are only 3.5-4 minutes of combined POES measurements included. In addition, our determination of calibration factors does not include an estimate of the uncertainty in the POES-reported fluxes. We assume that there is no consistent offset in the fluxes, such that random errors will be minimized through the SEA process. We note, however, that the *L*-shell limits are rather similar between the two approaches, especially when considering the zone of atmosphere affected (where changes of a few *L* at very high latitudes involve very small changes in latitude). Figure 7 shows a comparison between the IGRF L-shell limits for the *Berkey et al.* [1974] study, as well as the median substorm case and the poleward limit for the UQ substorms we determine.

7. Distribution of Substorm EEP magnitude

Given that there is clearly a wide variation in the observed EEP fluxes during substorms, we examine the statistical range of this parameter. Figure 8 shows a cumulative probability distribution of the >30 keV EEP fluxes from the POES spacecraft in the MLT range from 21-15 MLT. The >30 keV flux value is taken as the maximum flux in the *L*-shell range 6-7 and time range 0 to +2 hours from the epoch, i.e., the *L*-range and time period in which the EEP peaks. In this figure we show the distributions separately for each year 2005-2010, using the SuperMAG substorm lists for each of these years. We have excluded any time periods in which solar proton events occurred. For 2005 we only include substorms from 7 June 2005 onwards, to ensure there are sufficient spacecraft observations. The number of substorm events in each yearly list is given in the figure legend. Horizontal lines mark the lower and upper quartiles, and the median values. The years 2005-2008 and 2010 have very similar cumulative probability distributions despite very different substorm totals, and also have highly similar EEP median and quartile fluxes. In contrast, in 2009 there was both the smallest number of total substorms and these substorms were significantly weaker than in other years, with the median >30 keV precipitating flux being a factor of 3-4 times lower. The year 2009 also saw significantly lower solar wind speeds than the other years considered here. In that year solar wind speeds rarely exceeded 600 kms^{-1}, while in the other years we tend to see a bimodal distribution with a significant population above 550 kms^{-1}.

There have been a number of recent studies into substorms leading to large EEP fluxes [*Clilverd et al.*, 2008; 2012a; 2012b]. A reanalysis of the two large substorm events presented in *Clilverd et al.* [2008; 2012a] lead to peak EEP fluxes of ~1-3×10^7 el. $cm^{-2}s^{-1}sr^{-1}$ [*Rodger et* *al.*, 2012], while *Clilverd et al.* [2012b] reported on a substorm with fluxes of ~1-2×10^7 el. $cm^{-2}s^{-1}sr^{-1}$ observed by POES, which appears to have triggered the 9-month disruption in operations of the Galaxy-15 geostationary communications spacecraft. Figure 8 indicates that substorms producing fluxes of this magnitude passing through geostationary orbit (L≈6.6) are very rare. In the time period from 2007-2010 shown in Figure 8 the average probability of substorms with >30 keV EEP fluxes >10^7 el. $cm^{-2}s^{-1}sr^{-1}$ was 0.4%, i.e., approximately 1-6 times per year. Nonetheless, given that such events appear to be able to disable geostationary satellites when they are near midnight MLT, this comparatively small event rate still appears significant.

The year 2009 was remarkable in terms of energetic radiation belt fluxes. POES observations of trapped relativistic electrons (albeit at LEO) in the outer belt show near noise floor levels for most of the year, unprecedented in the ~14 years of SEM-2 observations. In the same time period the outer belt >100 keV POES trapped electron fluxes decreased by 1-1.5 orders of magnitude below their typical long term averages, only returning to normal in early 2010. These POES observations are consistent with the relativistic electron fluxes reported by SAMPEX [*Russell et al.*, 2010] at LEO and the geosynchronous GOES observations in the same time period. Figure 8 suggests that the number of substorms was not linked to the variation in energetic radiation belt fluxes as this is essentially the same in 2009 and 2010. However, we note that the substorms in 2009 are largely isolated events, separated in time by many hours, while in 2010 substorms tend to occur in short-lived clusters associated with periods of enhanced solar wind speeds. This deserves further examination.

8. Discussion

We have argued in this paper that the D-region enhancements observed by EISCAT Svalbard during the 2007-2008 IPY campaign were produced by substorms. Supportive evidence for this conclusion is provided by the MLT distribution of these IPY ESR events, the solar wind conditions, geomagnetic indices and geostationary particle injections associated with the events. In addition, of the 112 epochs in the IPY ESR event list, 75 occur within 0-2 hours of a SuperMAG reported substorm, i.e., are independently confirmed as substorms. For the rest of the 37 IPY ESR epochs which did not match the SuperMAG IPY substorm list, we have undertaken an additional SEA on the POES EEP observations. The POES EEP SEA for these 37 events are highly similar to the patterns and magnitudes seen in Figures 4 (for the entire 112 epoch list), and also Figure 5 (for the 1413 SuperMAG substorms). Thus we can conclude that these events are also likely to be substorm related, but further we suggest that SuperMAG may be missing as many as one-third of strong substorms (where strong is defined in terms of the strength of precipitation signature).

Substorm injection events were comprehensively mapped by *Berkey et al.* [1974] using about 40 northern hemisphere riometers in the IQSY (1964-1965) and IASY (1969). Initially the riometer absorption maximum was found to be located close to L~6 but expanded within 15 minutes to cover a range of L=4-10. In our study we have shown that the lower limit of the *Berkey et al.* [1974] study (L=4) is consistent with the lower L-shell limit of the strongest substorms examined in this study (i.e., L=4.1), suggesting that Berkey used the full range of substorm events in his analysis. The peak riometer absorption as a result of substorm EEP occurs at L=6-7, which is also consistent with the results of Berkey. The median peak riometer absorption at L=6-7 was estimated in our study to be 3.2 dB, which is consistent with the mean peak absorption reported by Berkey, again suggesting that the Berkey study used the full range of substorm events. However, the upper L-shell limit for weak and moderate substorms reported by Berkey was L=9.5, which is consistent with the upper L-shell range found in this study for only the weakest 25% of substorm samples (i.e., L=10.1±0.7). For substorms occurring during geomagnetically disturbed conditions (Kp>6) Berkey concluded that the poleward limit was typically about CGM 74° (with a local time dependence), which equates to an IGRF L-shell of ~15, consistent with our value for typical substorms (i.e.,

L=14.5±1.2). So what have we learned about substorms that we can use to explain the results of *Berkey et al.* [1974] in contrast to our own? In our study the upper boundary for median substorm events is L=14.5±1.2, and for the strongest 25% of events is L=20.7±2.2. The differences between the two studies are unlikely to be explained through our use of a calibration factor, which determines the uncertainties in our limit estimates. It is quite likely that a significant reason for the differences between the two studies arises from the distribution of riometers available to the authors of the *Berkey et al.* [1974] paper. As can be seen from Figure 1 and 2 of that paper, there were no riometer observations included between CGM latitudes of 75° to 80°, i.e. from approximately IGRF L=16 to L=35. Thus it seems possible that *Berkey et al.* [1974] may have struggled to adequately determine the poleward boundary for significant substorm EEP during the strongest events. Given the high variability in the EEP cutoffs from event to event it is also possible that the relatively small sample size of the *Berkey et al*. [1974] study (30 events) masked the typical behavior shown in our much larger analysis (1413 events).

9. Summary and Conclusions

In this study we have examined the latitudinal limits of substorm produced energetic electron precipitation (EEP) during quiet geomagnetic conditions. As the *Berkey et al.* [1974] study suggested substorm EEP affected a larger latitudinal range for geomagnetic disturbed conditions, our work may represent lower limits for the possible range likely for all conditions. Our attention was first triggered by the observations of significant D-region electron density enhancements observed during the IPY campaign by incoherent scatter radar at L≈16. The existing literature suggested that, outside of solar proton events, one would not typically expect significant EEP at such high latitudes, whether from substorms or the radiation belts. However, an examination of the MLT distribution of these events, as well as the IMF B_z, solar wind speed, geomagnetic indices and associated particle injection events at geostationary orbit indicated they were most likely triggered by substorms.

Therefore, we reexamined the latitudinal limits of substorm generated EEP using data from multiple low-Earth orbiting spacecraft and the SuperMAG substorm list, demonstrating that substorm EEP precipitation can regularly stretch many hundreds of kilometers polewards beyound the previously suggested limits (L=4–9.5). Using an approach linked to an earlier riometer-based study, we find that a typical substorm will produce significant EEP over the IGRF L-shell range L=4.6±0.2-14.5±1.2. Here we define a typical substorm through the median observed EEP for a SUPERMAG substorm event determined using SEA. However, there is substantial variability from event to event; in contrast to the median case, the strongest 25% of substorms have significant EEP in the range spaning L=4.1±0.1-20.7±2.2, while the weakest 25% of substorms have significant EEP in the range spaning L=5.5±0.1-10.1±0.7.

Finally, we examined the occurrence probability of very large substorms, defined in terms of the strength of their precipitation signature. We undertook this by examining the POES >30 keV precipitation fluxes for the substorms identified in the SuperMAG lists. The average probability of substorms with >30 keV EEP fluxes greater than 10^7 el. $cm^{-2}s^{-1}sr^{-1}$ was found to be 0.4%, i.e., approximately 1-6 times per year. Given that such events appear to be able to disable geostationary satellites when those spacecraft are located near midnight MLT, this comparatively small event rate is still important.

Acknowledgments. KCM and CJR were partly supported by the New Zealand Marsden Fund, while AK was supported by Finnish Academy project 134439 and TP was supported by the Väisälä Foundation. The authors would like to thank the researchers and engineers of NOAA's Space Environment Centre for the provision of the data and the operation of the SEM-2 instrument carried onboard these spacecraft. For the SuperMAG substorm lists we gratefully acknowledge: Intermagnet; USGS, Jeffrey J. Love; Danish Meteorological Institute; CARISMA, PI Ian Mann; CANMOS; The S-RAMP Database, PI K. Yumoto and Dr. K. Shiokawa; The SPIDR database; AARI, PI Oleg Troshichev; The MACCS program, PI M. Engebretson, Geomagnetism Unit of the Geological Survey of Canada; GIMA; MEASURE, UCLA IGPP and Florida Institute of Technology; SAMBA, PI Eftyhia Zesta; 210 Chain, PI K. Yumoto; SAMNET, PI Farideh Honary; The institutes who maintain the IMAGE magnetometer array, PI Eija Tanskanen; PENGUIN; AUTUMN, PI Martin Conners; Greenland magnetometers operated by DTU Space; South Pole and McMurdo Magnetometer, PI's Louis J. Lanzarotti and Alan T. Weatherwax; ICESTAR; RAPIDMAG; PENGUIn; British Artarctic Survey; McMac, PI Dr. Peter Chi; BGS, PI Dr. Susan Macmillan; Pushkov Institute of Terrestrial Magnetism, Ionosphere and Radio Wave Propagation (IZMIRAN); SuperMAG, PI Jesper W. Gjerloev. EISCAT is an international association supported by research organizations in China (CRIRP), Finland (SA), Germany (DFG, till end 2011), Japan (NIPR and STEL), Norway (NFR), Sweden (VR), and the United Kingdom (NERC).

References

Akasofu, S.-I. (1964), The development of the auroral substorm, Planet. Space. Sci., 12, 273-282, doi: 10.1016/0032-0633(64)90151-5.

Akasofu, S.-I. (1981), Energy coupling between the solar wind and magnetosphere disturbances, Space Sci. Rev., 28, 121.

Andersson, M. E., P. T. Verronen, S. Wang, C. J. Rodger, M. A. Clilverd, and B. R. Carson (2012), Precipitating radiation belt electrons and enhancements of mesospheric hydroxyl during 2004–2009, J. Geophys. Res., 117, D09304, doi:10.1029/2011JD017246.

Axford, W. (1999), Reconnection, substorms and solar flares, Physics and Chemistry of the Earth C, 24, 147-151, doi: 10.1016/S1464-1917(98)00022-1.

Berkey, F. T., Driatskiy, V. M., Henriksen, K., Hultqvist, B., Jelly, D. H., Shchuka, T. I., Theander, A., & Yliniemi, J. (1974), A Synoptic Investigation of Particle Precipitation Dynamics for 60 Substorms in IQSY (1964-1965) and IASY (1969). Planet. Space Sci., Vol. 22, pp. 255-307.

Brasseur, G., and S. Solomon (2005), Aeronomy of the Middle Atmosphere: Chemistry and Physics of the Stratosphere and Mesosphere, third ed., D. Reidel Publishing Company, Dordrecht.

Clilverd, M. A., A. Seppälä, C. J. Rodger, P. T. Verronen, and N. R. Thomson (2006), Ionospheric evidence of thermosphere-to-stratosphere descent of polar NOX, Geophys. Res. Lett., 33, L19811, doi:10.1029/2006GL026727.

Clilverd, M. A., C. J. Rodger, J. B. Brundell, N. Cobbett, J. Bähr, T. Moffat-Griffin, A. J. Kavanagh, A. Seppälä, N. R. Thomson, R. H. W. Friedel, and F. W. Menk (2008), Energetic electron precipitation during sub-storm injection events: high latitude fluxes and an unexpected mid-latitude signature, J. Geophys. Res., 113, A10311, doi: 10.1029/ 2008JA013220.

Clilverd, M A, C J Rodger, I J Rae, J B Brundell, N R Thomson, N Cobbett, P T Verronen, and F W Menk (2012a), Combined THEMIS and ground-based observations of a pair of substorm associated electron precipitation events, J. Geophys. Res., 117, A02313, doi:10.1029/2011ja016933.

Clilverd, M. A., C. J. Rodger, D. W. Danskin, M. E. Usanova, T. Raita, T. Ulich, and E. Spanswick (2012b), Energetic Particle injection, acceleration, and loss during the geomagnetic disturbances which upset Galaxy 15, J. Geophys. Res., 117, A12213, doi:10.1029/2012JA018175.

Connors, M., C. T. Russell, and V. Angelopoulos (2011), Magnetic flux transfer in the 5 April 2010 Galaxy 15 substorm: an unprecedented observation, Ann. Geophys., 29, 619-622, doi:10.5194/angeo-29-619-2011.

Evans, D. S., and M. S. Greer (2004), Polar Orbiting environmental satellite space environment monitor - 2 instrument descriptions and archive data documentation, NOAA technical Memorandum version 1.4, Space Environment Laboratory, Colorado.

Kofman, W., (1992), Auroral Ionospheric and Thermospheric Measurements using the Incoherent Scatter Technique, Surveys in Geophysics, 13: 551-571.

Lam, M. M., R. B. Horne, N. P. Meredith, S. A. Glauert, T. Moffat-Griffin, and J. C. Green (2010), Origin of energetic electron precipitation >30 keV into the atmosphere, J. Geophys. Res., 115, A00F08, doi:10.1029/2009JA014619.

Liu, J., V. Angelopoulos, H. Frey, J. McFadden, D. Larson, K. Glassmeier, S. Mende, C. T. Russell, I. J. Rae, K. R. Murphy, and S. Apatenkov (2009), THEMIS observation of a substorm event on 04:35, 22 February 2008, Ann. Geophys., 27, 1831-1841, doi:10.5194/angeo-27-1831-2009.

Liu, W. W., J. Liang, E. F. Donovan, and E. Spanswick (2012), If substorm onset triggers tail reconnection, what triggers substorm onset?, J. Geophys. Res., 117, A11220, doi:10.1029/2012JA018161.

Mende, S. B., C. W. Carlson, H. U. Frey, L. M. Peticolas, and N. Østgaard (2003), FAST and IMAGE-FUV observations of a substorm onset, J. Geophys. Res., 108(A9), 1344, doi:10.1029/2002JA009787.

Newell, P. T., and J. W. Gjerloev (2011a), Evaluation of SuperMAG auroral electrojet indices as indicators of substorms and auroral power, J. Geophys. Res., 116, A12211, doi:10.1029/2011JA016779).

Newell, P. T., and J. W. Gjerloev (2011b), Substorm and magnetosphere characteristic scales inferred from the SuperMAG auroral electrojet indices, J. Geophys. Res., 116, A12232, doi:10.1029/2011JA016936.

Newnham, D. A., P. J. Espy, M. A. Clilverd, C. J. Rodger, A. Seppälä, D. J. Maxfield, P. Hartogh, K. Holmén, and R. B. Horne (2011), Direct observations of nitric oxide produced by energetic electron precipitation in the Antarctic middle atmosphere, Geophys. Res. Lett., 38(20), L20104, doi:10.1029/2011GL049199.

Nishimura, Y., L. Lyons, S. Zou, V. Angelopoulos, and S. Mende (2010), Substorm triggering by new plasma intrusion: THEMIS all-sky imager observations, J. Geophys. Res., 115, A07222, doi:10.1029/2009JA015166.

Randall, C. E., V. L. Harvey, C. S. Singleton, S. M. Bailey, P. F. Bernath, M. Codrescu, H. Nakajima, and J. M. Russell (2007), Energetic particle precipitation effects on the Southern Hemisphere stratosphere in 1992–2005, J. Geophys. Res., 112, D08308, doi:10.1029/2006JD007696.

Robel, J. (Ed.), NOAA KLM User's Guide, National Environmental Satellite, Data, and Information Service, 2009.

Rodger, C. J., M. A. Clilverd, J. Green, and M.-M. Lam (2010a), Use of POES SEM-2 observations to examine radiation belt dynamics and energetic electron precipitation in to the atmosphere, J. Geophys. Res., 115, A04202, doi: 10.1029/2008JA014023.

Rodger, C. J., B. R. Carson, S. A. Cummer, R. J. Gamble, M. A. Clilverd, J-A. Sauvaud, M. Parrot, J. C. Green, and J.-J. Berthelier (2010b), Contrasting the efficiency of radiation belt losses caused by ducted and non-ducted whistler mode waves from ground-based transmitters, J. Geophys. Res., 115, A12208, doi:10.1029/2010JA015880.

Rodger, C J, M A Clilverd, A J Kavanagh, C E J Watt, P T Verronen, and T Raita (2012), Contrasting the responses of three different ground-based instruments to energetic electron precipitation, Radio Sci., 47(2), RS2021, doi:10.1029/2011RS004971.

Rostoker, G., Akasofu, S.-I., Foster, J., Greenwald, R. A., Kamide, Y., Kawasaki, K., Lui, A. T. Y., McPherron, & R. L., Russell, C. T. (1980), Magnetospheric Substorms – Definition and Signatures, J. Geophys. Res., Vol. 85, No. A4, pp. 1663-1668.

Rozanov, E., L. Callis, M. Schlesinger, F. Yang, N. Andronova, and V. Zubov (2005), Atmospheric response to NOy source due to energetic electron precipitation, Geophys. Res. Lett., 32, L14811, doi:10.1029/2005GL023041.

Russell, C. T., J. G. Luhmann, and L. K. Jian (2010), How unprecedented a solar minimum?, Rev. Geophys., 48, RG2004, doi:10.1029/2009RG000316.

Sandholt, P. E., C. J. Farrugia, M. Lester, S. Cowley, S. Milan, W. F. Denig, B. Lybekk, E. Trondsen, and V. Vorobjev (2002), Multistage substorm expansion: Auroral dynamics in relation to plasma sheet particle injection, precipitation, and plasma convection, J. Geophys. Res., 107(A11), 1342, doi:10.1029/2001JA900116.

Sarris, T. and Li, X. (2005), Evolution of the dispersionless injection boundary associated with substorms, Ann. Geophys., 23, 877-884, doi:10.5194/angeo-23-877-2005.

Seppälä, A., M. A. Clilverd, and C. J. Rodger (2007), NOx enhancements in the middle atmosphere during 2003-2004 polar winter: Relative significance of solar proton events and the aurora as a source, J. Geophys. Res., D23303, doi:10.1029/2006JD008326.

Seppälä, A., C. E. Randall, M. A. Clilverd, E. Rozanov, and C. J. Rodger (2009), Geomagnetic activity and polar surface level air temperature variability, J. Geophys. Res., 114, A10312, doi:10.1029/2008JA014029.

Sergeev, V. A., I. A. Chernyaev, S. V. Dubyagin, Y. Miyashita, V. Angelopoulos, P. D. Boakes, R. Nakamura, and M. G. Henderson (2012), Energetic particle injections to geostationary orbit: Relationship to flow bursts and magnetospheric state, *J. Geophys. Res.*, 117, A10207, doi:10.1029/2012JA017773.

Smith, A., M. Freeman, and G. Reeves (1996), Post midnight VLF chorus events, a substorm signature observed at the ground near L=4, J. Geophys. Res., 101(A11), 24641-24653.

Spanswick, E., et al. (2009), Global observations of substorm injection region evolution: 27 August 2001, Ann. Geophys., 27, 2019-2025.

Tanskanen, E. I., J. A. Slavin, A. J. Tanskanen, A. Viljanen, T. I. Pulkkinen, H. E. J. Koskinen, A. Pulkkinen, and J. Eastwood (2005), Magnetospheric substorms are strongly modulated by interplanetary high-speed streams, Geophys. Res. Lett., 32, L16104, doi:10.1029/2005GL023318.

Turunen, E., P. T. Verronen, A. Seppälä, C. J. Rodger, M. A. Clilverd, J. Tamminen, C. F. Enell and Th. Ulich (2009), Impact of different precipitation energies on NOx generation during geomagnetic storms, J. Atmos Sol.-Terr. Phys., 71, pp. 1176-1189, doi:10.1016/j.jastp.2008.07.005.

Watson, C., P. T. Jayachandran, E. Spanswick, E. F. Donovan, and D. W. Danskin (2011), GPS TEC technique for observation of the evolution of substorm particle precipitation, J. Geophys. Res., 116, A00I90, doi:10.1029/2010JA015732.

Verronen, P. T., C. J. Rodger, M. A. Clilverd, and S. Wang (2011), First evidence of mesospheric hydroxyl response to electron precipitation from the radiation belts, J. Geophys. Res., 116, D07307, doi:10.1029/2010JD014965.

M. A. Clilverd, British Antarctic Survey, High Cross, Madingley Road, Cambridge CB3 0ET, England, U.K. (e-mail: macl@bas.ac.uk).

A. B. Collier, SANSA Space Science, PO Box 32, Hermanus 7200, South Africa. (collierab@gmail.com)

K. Cresswell-Moorcock and C. J. Rodger, Department of Physics, University of Otago, P.O. Box 56, Dunedin, New Zealand. (email: crodger@physics.otago.ac.nz).

Ingemar Häggström, EISCAT Scientific Association, Box 812, SE-98128 Kiruna, Sweden. (email: ingemar@eiscat.se).

T. Pitkänen, Department of Physics, University of Oulu, P.O.Box 3000, FI-9001, Finland. (email: timo.pitkanen@oulu.fi).

A. Kero, Sodankylä Geophysical Observatory, University of Oulu, Sodankylä, Finland. (email: Antti.Kero@sgo.fi)

CRESSWELL-MOORCOCK ET AL.: SUBSTORM EEP GEOMAG. LATITUDE LIMITS

Tables

Satellite	Local Time Ascending Node	Altitude (km)	Data availability
NOAA 15	16:42:14	807	01 June 1998
NOAA 16	20:28:56	849	10 January 2001
NOAA 17	19:12:50	810	12 July 2002
NOAA 18	14:51:13	854	07 June 2005
MetOp 02	21:30:22	817	03 December 2006
NOAA 19	13:33:02	870	23 February 2009

Table 1. An overview of the six satellites carrying the SEM-2 instrument package, including their daytime orbital sector, and date at which they became operational. Note MetOp-2 is a European spacecraft, but carries the same SEM-2 package as the NOAA spacecraft. The local time ascending node is the local time for which the spacecraft are crossing the equator travelling northwards.

Data Channel	Observes
0E1	>30 keV e^-
0E2	>100 keV e^-
0E3	>300 keV e^-
0P1	52 keV diff. p^+
0P2	138 keV diff. p^+
0P3	346 keV diff. p^+
0P4	926 keV diff. p^+
0P5	2628 keV diff. p^+

Table 2. Detectors which are part of the POES SEM-2 MEPED instrument used in the current study. The telescopes are ±15º wide.

Figures

Figure 1. Map showing the location of the EISCAT Svalbard Radar (ESR) and the limits for substorm (blue lines) and radiation belt EEP (red lines).

Figure 2. Superposed epoch analysis of the electron density increases observed by the EISCAT Svalbard Radar facility during the IPY continuous observation period. Left hand panel shows the mean while the right hand panel shows the median.

Figure 3. Characteristics of the IPY ESR electron number density increase events. The left hand panel shows the distribution with Magnetic Local Time (MLT), while the right hand panel shows a superposed epoch analysis of the *z*-component of the Interplanetary Magnetic Field (IMF B_z). Here the superposed epoch median of the IMF B_z is given by a black line. The 95% confidence interval for the median is given by the red band. The dark blue bands mark the interquartile range and the 95% confidence interval about it (light blue).

Figure 4. Superposed epoch analysis of median POES >30 keV precipitating electrons for the IPY ESR epochs. The left hand panel shows the variation in the precipitating fluxes, while the right hand panel shows the changes relative to a SEA of random epoch times. In both cases the *L*-shell of the ESR is marked by the horizontal dotted white line.

Figure 5. Superposed epoch analysis of median POES >30 keV precipitating electrons for the IPY SuperMAG substorm epochs, for 4 different MLT ranges (±3 hours).

Figure 6. Determining the IGRF *L*-shell limits of significant substorm EEP, based on the *Berkey et al.* [1974] threshold of 0.3 dB (magenta dashed line). The lefthand panel uses the

"calibration factor" determined by the ESR and POES observations, while the righthand panel uses a "calibration factor" determined from the typical substorm intensities reported by *Berkey et al.* [1974] (as explained in the text). The blue line is the riometer absorption change (ΔCNA) for the median >30 keV EEP calculations, while the red line is for the upper quartile (UQ) and the green line is the lower quartile (LQ) EEP calculations. The vertical blue dashed lines mark the limits for the typical (median) case.

Figure 7. Map showing the location of the EISCAT Svalbard Radar (ESR) and the limits for substorm produced EEP. The blue show the poleward (cross markers) and equatorward (dashed) limits for substorm-EEP determined by *Berkey et al.* [1974] from riometer data. The red show the typical (median) substorm satellite-determined limits found in this study, in the same format. The magenta gives the upper quartile (UQ) substorm EEP limits found in this study.

Figure 8. Cumulative probability distribution of the >30 keV EEP fluxes observed by the POES spacecraft in the MLT range 21-15 for L=6-7 and 0-2 hours after the epoch for each SuperMAG substorm. The number of substorm events in each year is given in the figure legend. Note that the 2005 analysis starts from 7 June 2005 as outlined in the text.

Figures

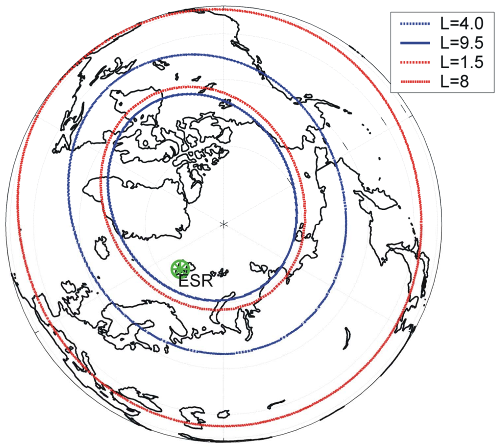

Figure 1. Map showing the location of the EISCAT Svalbard Radar (ESR) and the limits for substorm (blue lines) and radiation belt EEP (red lines).

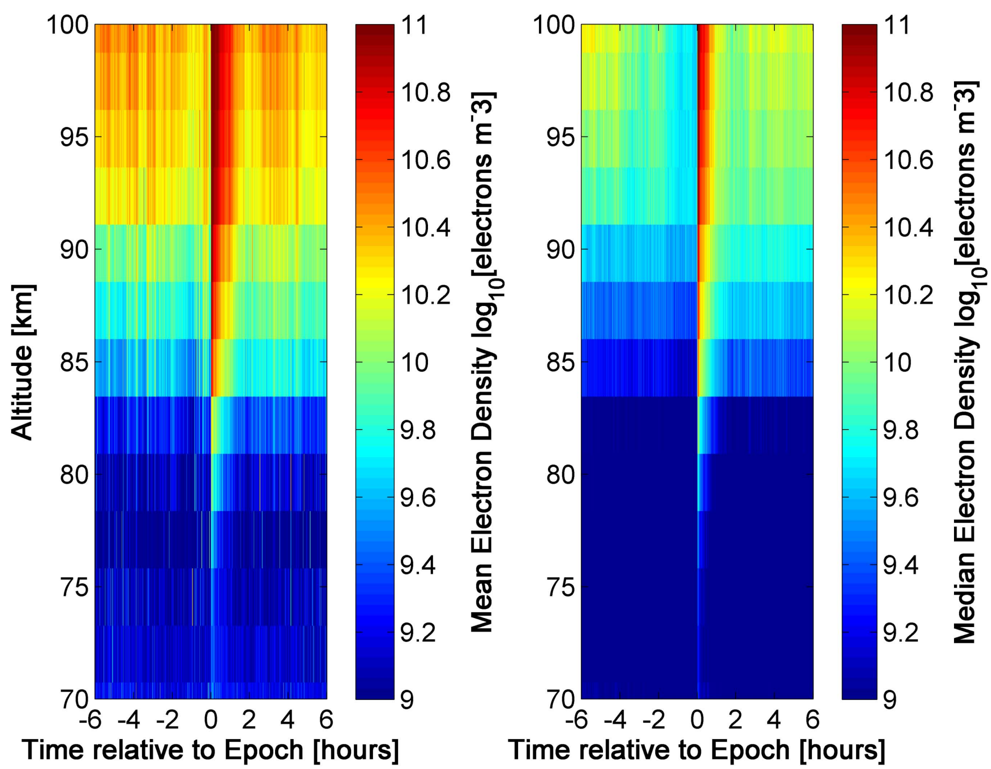

Figure 2. Superposed epoch analysis of the electron density increases observed by the EISCAT Svalbard Radar facility during the IPY continuous observation period. Left hand panel shows the mean while the right hand panel shows the median.

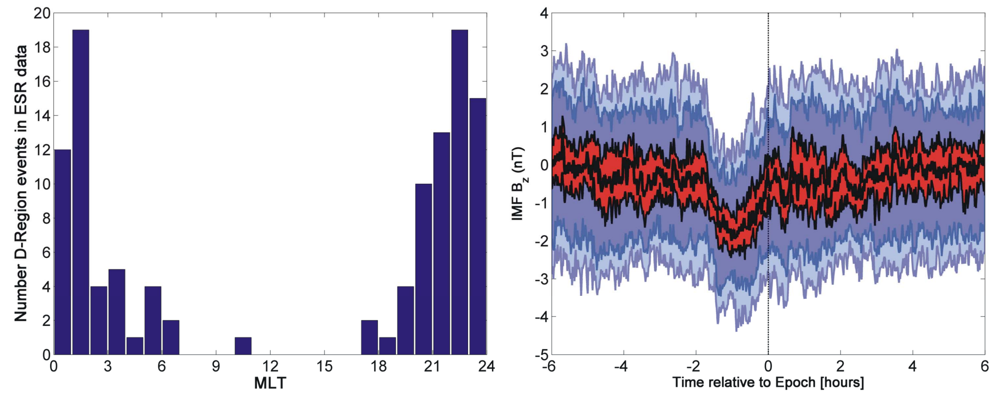

Figure 3. Characteristics of the IPY ESR electron number density increase events. The left hand panel shows the distribution with Magnetic Local Time (MLT), while the right hand panel shows a superposed epoch analysis of the *z*-component of the Interplanetary Magnetic Field (IMF B_z). Here the superposed epoch median of the IMF B_z is given by a black line. The 95% confidence interval for the median is given by the red band. The dark blue bands mark the interquartile range and the 95% confidence interval about it (light blue).

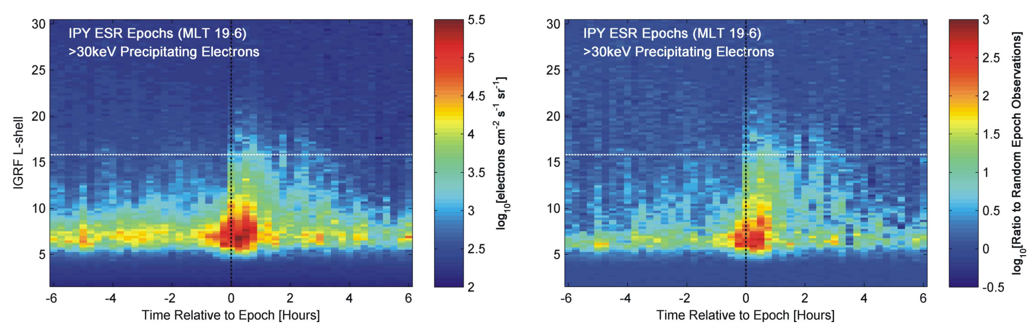

Figure 4. Superposed epoch analysis of median POES >30 keV precipitating electrons for the IPY ESR epochs. The left hand panel shows the variation in the precipitating fluxes, while the right hand panel shows the changes relative to a SEA of random epoch times. In both cases the *L*-shell of the ESR is marked by the horizontal dotted white line.

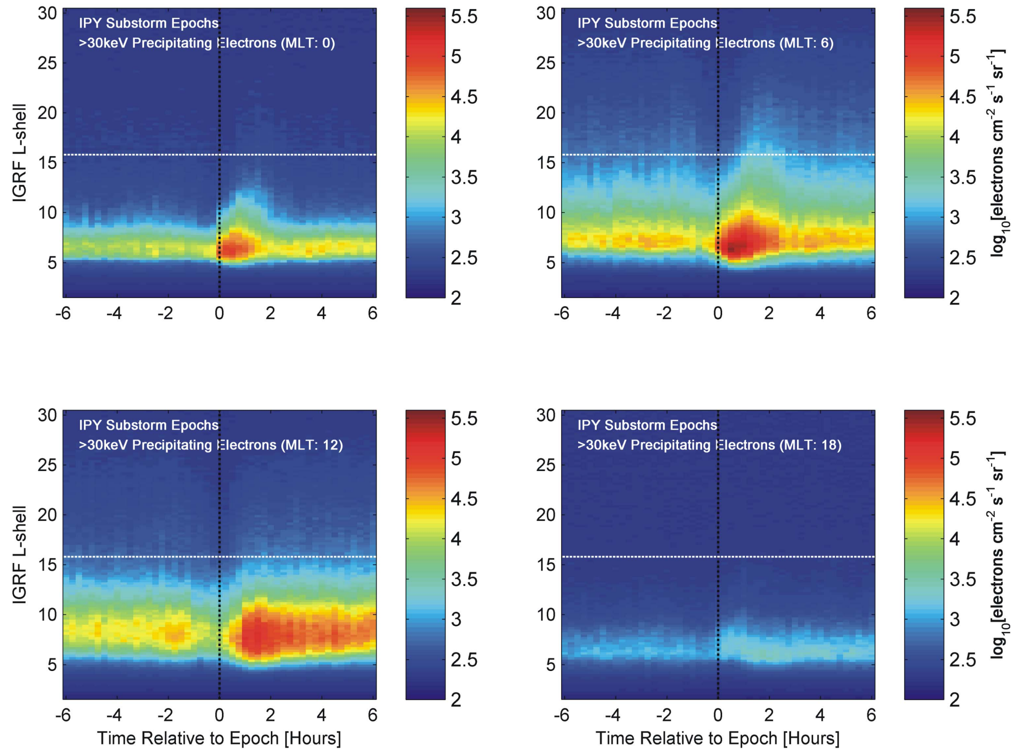

Figure 5. Superposed epoch analysis of median POES >30 keV precipitating electrons for the IPY SuperMAG substorm epochs, for 4 different MLT ranges (±3 hours).

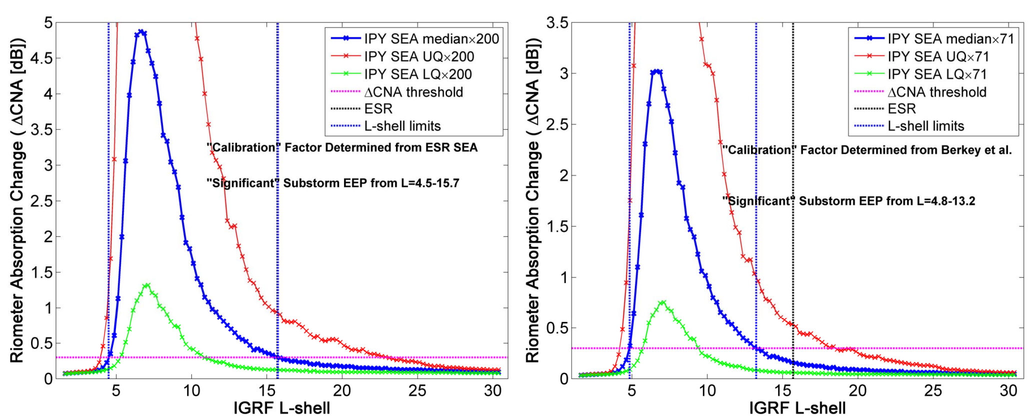

Figure 6. Determining the IGRF *L*-shell limits of significant substorm EEP, based on the *Berkey et al.* [1974] threshold of 0.3 dB (magenta dashed line). The lefthand panel uses the "calibration factor" determined by the ESR and POES observations, while the righthand panel uses a "calibration factor" determined from the typical substorm intensities reported

by *Berkey et al.* [1974] (as explained in the text). The blue line is the riometer absorption change (ΔCNA) for the median >30 keV EEP calculations, while the red line is for the upper quartile (UQ) and the green line is the lower quartile (LQ) EEP calculations. The vertical blue dashed lines mark the limits for the typical (median) case.

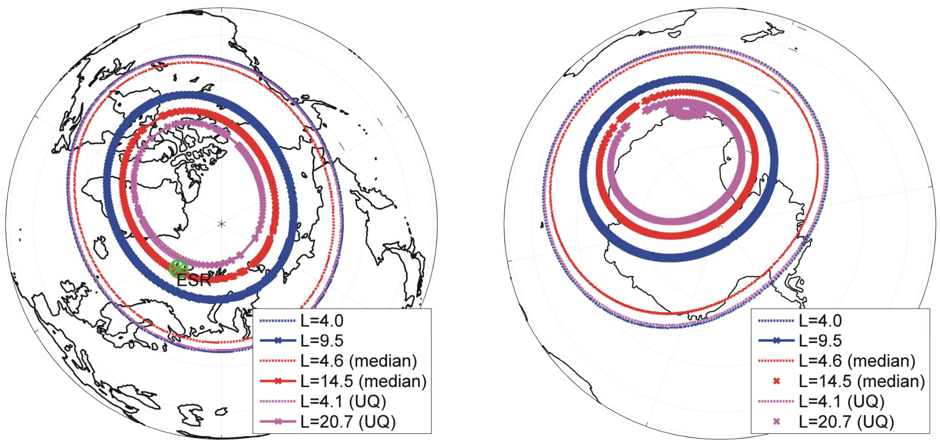

Figure 7. Map showing the location of the EISCAT Svalbard Radar (ESR) and the limits for substorm produced EEP. The blue show the poleward (cross markers) and equatorward (dashed) limits for substorm-EEP determined by *Berkey et al.* [1974] from riometer data. The red show the typical (median) substorm satellite-determined limits found in this study, in the same format. The magenta gives the upper quartile (UQ) substorm EEP limits found in this study.

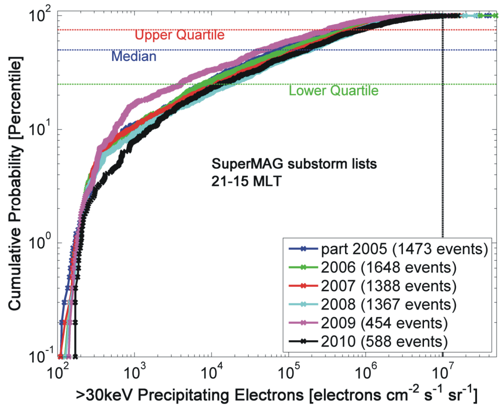

Figure 8. Cumulative probability distribution of the >30 keV EEP fluxes observed by the POES spacecraft in the MLT range 21-15 for *L*=6-7 and 0-2 hours after the epoch for each SuperMAG substorm. The number of substorm events in each year is given in the figure legend. Note that the 2005 analysis starts from 7 June 2005 as outlined in the text.